

Additional Magnetic Field of Dual-parallel Rotor Permanent Magnet Synchronous Motor and Its Influence on Electromagnetic Torque

Yang Chen, *Student Member, CES*, Dajun Tao, and Baojun Ge

Abstract—The coupling effect of dual-parallel rotor connected stator permanent magnet synchronous motor not only affects the magnetic field in the coupling area, but also generates an additional magnetic field in the uncoupled area. The characteristics of the additional magnetic field and its influence on electromagnetic torque are studied in this paper. The topology and parameters of motor are described briefly. The existence of additional magnetic field is proved by the simulation models under two boundary conditions, and its characteristics and source are analyzed. The analytical model is established, and the influence of key parameters on the additional magnetic field is discussed. On this basis, the influence of the additional magnetic field on the electromagnetic torque of the motor is studied, and the analytical expression of the additional torque is constructed. The fluctuation rule is analyzed, and the additional magnetic field separation model is proposed. The theoretical analysis and simulation results reveal and improve the internal mechanism of reducing motor torque ripple by optimizing the duty angle and coupling distance. Finally, a prototype test platform is built to verify the correctness of the proposed theory and the accuracy of the simulation model.

Index Terms—Dual-parallel rotor, Permanent magnet motor, Connected stator, Additional magnetic field.

I. INTRODUCTION

IN parallel-to-drive mechanical equipment such as double screw pump, twin screw compressor, two-high mill and roll crusher, etc., the current driving mode is still master-slave driving by single motor as the mainstream. A motor transmits the torque to the drive shaft through the coupling, gear box and other transmission links, and the drive shaft drives the driven shaft to rotate through the mechanical synchronous gear between the drive shaft and driven shaft, so as to realize the reverse synchronous rotation of the two shafts. This

driving mode has some problems, such as large equipment volume, low system efficiency, large mechanical noise, difficult sealing, and regular maintenance [1]-[2]. In addition, the single motor is mostly driven by induction motor and gearbox transmission [3]-[5], resulting in a large energy loss in the entire transmission system. Although the direct drive method of permanent magnet motor is proposed to improve the system efficiency to a certain extent [6]-[8], the problem of parallel-to-drive mechanical equipment cannot be fundamentally solved due to the existence of synchronous gears.

In order to solve the problems of the above-mentioned driving mode, the dual-parallel rotor connected stator permanent magnet synchronous motor (DRCS-PMSM) has gradually attracted the attention of experts and scholars, which can directly drive parallel-to-drive mechanical equipment. This driving mode can eliminate the redundant links of the whole transmission system, and has the advantages of small system volume, high system efficiency, gearless transmission, good synchronization of two shafts, and low mechanical noise.

DRCS-PMSM can be regarded as a splice of two conventional motors after cutting off part of their stators. [9] presents a topology with similar structure to DRCS-PMSM and studies the design method of this type of motor. [1] uses the subdomain method to analyze and calculate the no-load magnetic field of the motor proposed in reference [9]. On this basis, the authors' team have studied the torque ripple mechanism and suppression method of DRCS-PMSM in [10]. Besides, the unbalanced electromagnetic force on the rotor is also analyzed and optimized [11]-[12].

According to [2] and [9], the no-load torque of DRCS-PMSM is composed of three components, namely, teeth-slot torque, end effect torque and permanent magnet gear transmission torque. However, a recent study by the authors' team found that the end effect and magnetic gear effect not only affect the air gap magnetic field at the end, but also have a certain impact on the air gap magnetic field at the non-end. In this paper, the component that causes the change of the non-end air gap magnetic field is defined as the additional magnetic field. The field further affects the electromagnetic torque of DRCS-PMSM, thus affecting the smooth operation of the motor. Therefore, it is of great academic significance and engineering value to study the additional magnetic field

Manuscript received February 16, 2025; revised March 10, 2025; accepted April 14, 2025. Date of publication June 25, 2025; Date of current version May 06, 2025.

This work was supported in part by the Natural Science Foundation of Heilongjiang Province under Grant LH2023E084, and by the National Natural Science Foundation of China under Grant 51777048. (*Corresponding Author: Dajun Tao*)

Yang Chen, Dajun Tao, and Baojun Ge are with School of Electrical and Electronic Engineering, Harbin University of Science and Technology, Harbin 150080, China (e-mail: chenyang2022@foxmail.com; tao.dj@163.com; gebj@hrbust.edu.cn).

Digital Object Identifier 10.30941/CESTEMS.2025.00015

of DRCS-PMSM and reveal its influence on electromagnetic torque, which can improve the torque ripple theory of DRCS-PMSM.

Most studies on the air-gap magnetic field of motors focus on the analytical calculation of the air-gap magnetic field [13]-[16]. When linear motor is taken as the research object, special consideration should be given to the asymmetry of windings and the end effect of stator core [17]-[20]. As for the research on additional magnetic field in the air gap, the [21] reveals that in permanent magnet linear motor, the pulsating magnetic field exists in the non-end air gap magnetic field in the form of DC component due to the “magnetic aggregation effect” of the end core, and its amplitude changes with the change of the primary and secondary relative positions. However, this study only selected the magnetic field corresponding to a pair of poles in the center of the non-end air gap as the object, and the law of the additional magnetic field at other positions in the non-end air gap is not yet known. The above research results have important guiding significance for the research of additional magnetic field in DRCS-PMSM air gap in this paper.

The purpose of this research is to analyze the source and characteristics of the additional magnetic field in the DRCS-PMSM air gap, and to find out the effect of the additional magnetic field on the electromagnetic torque, so as to provide theoretical support for the high-performance design of DRCS-PMSM. The rest of the paper is as follows: Section II describes the topology and parameters of DRCS-PMSM. In section III, the existence of additional magnetic field in DRCS-PMSM is proved by establishing finite element simulation models under two boundary conditions. Section IV analyzes the characteristics of the additional magnetic field, explores its source and establishes an analytical model to study the influence of key parameters on the additional magnetic field. Section V further explores the effect of the additional magnetic field on DRCS-PMSM electromagnetic torque. In Section VI, a prototype is developed and a test platform is built to verify the reliability of the proposed theory and the accuracy of the finite element model.

II. TOPOLOGY AND PARAMETERS OF DRCS-PMSM

The topological structure of DRCS-PMSM is shown in Fig. 1. Fig. 1(a) is the overall structure of the motor, and Fig. 1(b) is the electromagnetic structure. DRCS-PMSM can be regarded as a splice of two conventional motors after cutting part of their stator. The overall structure is composed of two rotating shafts, a connected stator core with two sets of windings, two rotors, a shell, two end caps and other components. The electromagnetic structure of DRCS-PMSM consists of a connected stator core, two sets of windings on the left and right sides, and two rotors on the left and right sides. The two rotors adopt a surface mounted permanent magnet rotor structure. Permanent magnets are evenly distributed on the rotor core. The polarity of the permanent

magnets in adjacent positions of a single rotor is opposite, and the polarity of the permanent magnets in symmetrical positions along the vertical center line of the motor is opposite.

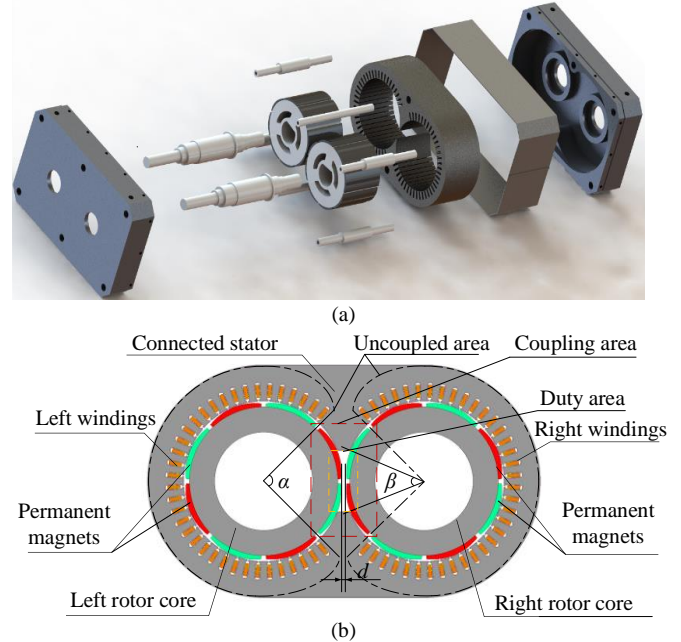


Fig. 1. Topological structure of DRCS-PMSM. (a) Overall structure. (b) Electromagnetic structure.

The area without windings distribution of the stator core is defined as the coupling area, and the central angle of the coupling area is the coupling angle, represented by the letter α . The area without stator core in the coupling area is defined as the duty area, and the central angle of the duty area is the duty angle, represented by the letter β . The minimum distance between two permanent magnet rotors is defined as the coupling distance, which is represented by the letter d . The above structural parameters are unique to DRCS-PMSM, and their sizes affect the magnetic circuit distribution in the motor coupling area, and thus affect the motor performance. The uncoupled area is the part surrounded by the black dashed line in Fig. 1(b). This effect is caused by the end effect caused by the breaking of the stator core and the magnetic gears effect between the two permanent magnet rotors, which are collectively referred to as “coupling effect” in this paper for convenience.

For the single-sided motor of DRCS-PMSM, the missing stator is one or more unit-motors, so the remaining windings of the single-sided motor are still three-phase symmetrical windings. The reason why a single-sided motor can operate is very similar to a conventional linear or arc motor. When two sets of windings are symmetrically excited with three phases, two oppositely rotating magnetic fields are generated in two air gaps, and the two magnetic fields interact with their respective rotors, so as to realize the reverse synchronous rotation of the two rotors. This paper takes DRCS-PMSM for twin-screw pump as the background, and the rated data and structural parameters of DRCS-PMSM studied are shown in Table I.

TABLE I
RATED DATA AND STRUCTURAL PARAMETERS OF DRCS-PMSM

Parameters	Value
Rated power/kW	11
Rated voltage/V	380
Frequency/Hz	50
Rated speed/(r min ⁻¹)	750
Shaft pitch/mm	180
Coupling angle/(°)	90
Duty angle/(°)	45
Air gap length/mm	0.8
Stator outside diameter/mm	260
Stator inner diameter/mm	180
Rotor inner diameter/mm	110
Laminated length/mm	120
Number of windings layers	1
Number of parallel branches	1
Number of stator slots	36×2
Coupling distance/mm	1.6

III. ADDITIONAL MAGNETIC FIELD OF DRCS-PMSM

A. Finite Element Models under Two Boundary Conditions

In order to facilitate the analysis, the influence of stator slots on the air gap magnetic field is ignored, that is, the influence of teeth-slot effect is ignored. The slot-less finite element simulation models are established under two boundary conditions: master-slave boundary and vector magnetic potential boundary, as shown in Fig. 2. Fig. 2(a) shows master-slave boundary model, which is similar to the conventional permanent magnet motor model, and does not have “coupling effect”. The magnetic vector of the master boundary is opposite to that of the slave boundary. Fig. 2(b) shows the vector magnetic potential boundary model. The vector magnetic potential is set to 0, that is, no magnetic flux lines cross the boundary. This model in Fig. 2(b) has a “coupling effect”. By comparing and analyzing the radial air-gap magnetic flux density of the simulation models under two boundary conditions, the variation of the air-gap magnetic field caused by the “coupling effect” can be obtained.

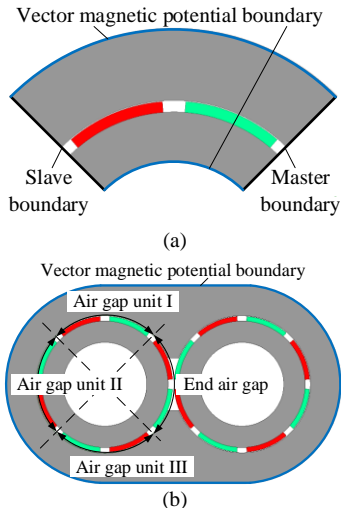


Fig. 2. Finite element simulation models. (a) Master-slave boundary. (b) Vector magnetic potential boundary.

Due to the structure symmetry of DRCS-PMSM, the air gap in the slotted stator of the left motor is selected as the research object. The sampling line of the magnetic flux density of the air gap is the center line of the air gap, and its variation in the radial direction is ignored. The coupling area makes the magnetic circuit of the motor asymmetrical. The air gap in the slotted stator is divided into three units, and each unit corresponds to a pair of permanent magnets, which are called air gap unit I, air gap unit II and air gap unit III. Each air gap unit is studied separately. The air gap in the coupling area is called the end air gap. The additional magnetic flux density $B_{r0,i}$ in the i -th air gap unit can be expressed as:

$$B_{r0,i}(\theta, x) = B_{r1}(\theta, x) - B_{r2,i}(\theta, x), \quad i = \text{I, II, III} \quad (1)$$

where B_{r1} is the magnetic flux density of the air gap in the master-slave boundary model. $B_{r2,i}$ is the magnetic flux density of the i -th air gap unit in the vector magnetic potential boundary model. θ is the rotor initial position. x is the relative position between the stator and the rotor.

B. Proof of Existence of Additional Magnetic Field

Two typical moments ($t=0$ ms and $t=5$ ms) are taken to calculate the finite element models under two boundary conditions. When $t=0$ ms, the relative position of the stator and the rotor is shown in Fig. 2. When $t=5$ ms, the rotor just turns half pole distance 0.5τ . The radial air gap magnetic flux density simulation results at two typical moments are shown in Fig. 3. The burrs in the waveform may be caused by uneven mesh division or inappropriate step size. As can be seen from Fig. 3, no matter which air gap unit, the radial air gap magnetic flux density waveform of the model under the two boundary conditions does not completely coincide. Especially when $t=5$ ms, it can be clearly seen that there is a bias between the two waveforms, which reflects the change of the DRCS-PMSM air gap magnetic flux density caused by the “coupling effect”.

According to (1), the magnetic flux density curves of the additional magnetic fields of different air gap units at two typical moments of DRCS-PMSM are shown in Fig. 4. The burrs in the curves are caused by the superposition of burrs in Fig. 3, but it is still obvious that the additional magnetic field has a certain periodicity. The effective values of the additional magnetic flux density of different air gap units are calculated and harmonic analysis of the additional magnetic flux density is carried out. The results are shown in Fig. 5. As can be seen from Fig. 5, the effective values of additional magnetic flux density are different in different air gap units at the same moment, and The effective value of the additional magnetic flux density in the air gap unit II is the largest. With the change of the relative position of the stator and the rotor, the DC component appears in the air-gap magnetic field, and the DC component in each air-gap unit is approximately equal. The additional magnetic flux density is periodic along the circumference of the air gap, and its fundamental wave frequency is exactly twice the pole distance 2τ . The fundamental wave amplitude of each air gap unit is different and changes with the relative position of the stator and the

rotor, among which the fundamental wave amplitude of the additional magnetic flux density of air gap unit II is the largest.

The above analysis proves the existence of additional magnetic field in DRCS-PMSM. It should be noted that the air gap unit I and the air gap unit III are closer to the coupling area, and they are more affected by the ‘‘coupling effect’’. Even though the air gap unit II is located in the middle of the stator core, it is far away from the coupling area, but it is still affected by the ‘‘coupling effect’’.

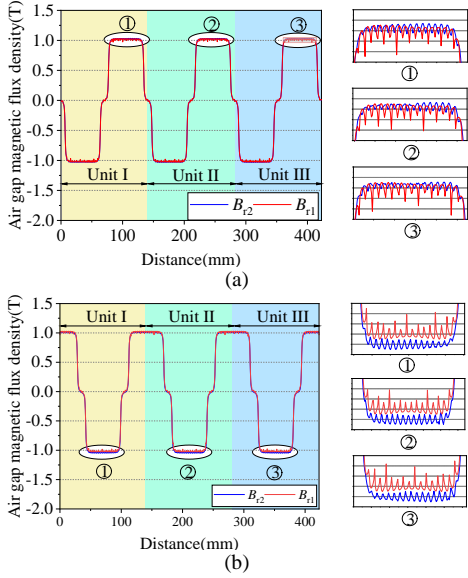


Fig. 3. Radial air gap magnetic flux density at two typical moments. (a) $t=0$ ms. (b) $t=5$ ms.

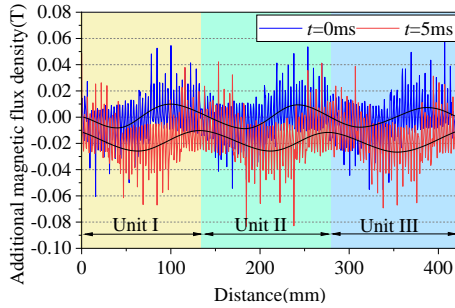


Fig. 4. Additional magnetic flux density at two typical moments.

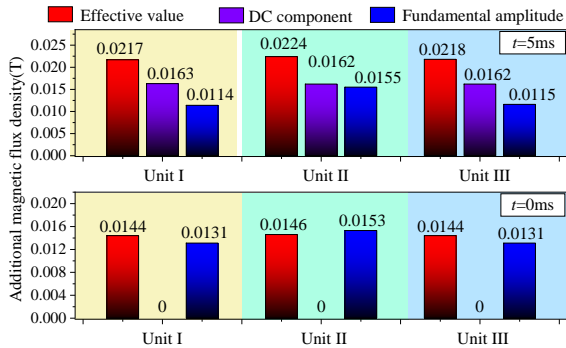


Fig. 5. Effective value and harmonic analysis of additional magnetic flux density.

C. The Distribution Laws of the Additional Magnetic Field

The rated frequency of DRCS-PMSM is 50 Hz, and the

time t used by the rotor to rotate a pair of poles is 20 ms. According to the analysis method of additional magnetic field in Section B, the additional magnetic flux density of different air gap units at different times within 0-20 ms is calculated, and harmonic analysis is performed. The results obtained are summarized in Table II, where B_{r0dc} represents the DC component and B_{r01} represents the fundamental wave amplitude. It can be seen from Table II that at the same time, the DC component B_{r0dc} of the additional magnetic flux density of different air gap units is basically the same, and with the change of time, the DC component B_{r0dc} first increases and then decreases, and then increases reversely and then decreases. In terms of fundamental amplitude B_{r01} , the values of B_{r01} of air gap unit I and air gap unit III are basically the same, and with the change of time, there is a law of first decreasing and then increasing, and then decreasing and then increasing again. The B_{r01} of air gap unit II can be regarded as a constant value, which does not change with time.

TABLE II
ADDITIONAL MAGNETIC FLUX DENSITY OF DIFFERENT AIR GAP UNITS AT DIFFERENT TIMES

t (ms)	Air gap unit I		Air gap unit II		Air gap unit III	
	$B_{r0dc,I}$ (T)	$B_{r01,I}$ (T)	$B_{r0dc,II}$ (T)	$B_{r01,II}$ (T)	$B_{r0dc,III}$ (T)	$B_{r01,III}$ (T)
0	0	0.0131	0	0.0153	0	0.0131
3	0.0094	0.0125	0.0092	0.0153	0.0093	0.0124
5	0.0163	0.0114	0.0162	0.0155	0.0162	0.0115
7	0.0093	0.0125	0.0092	0.0153	0.0092	0.0123
10	0	0.0132	0	0.0152	0	0.0130
13	-0.0093	0.0125	-0.0092	0.0155	-0.0092	0.0127
15	-0.0163	0.0113	-0.0161	0.0153	-0.0162	0.0114
17	-0.0093	0.0126	-0.0092	0.0155	-0.0092	0.0125
20	0	0.0131	0	0.0153	0	0.0130

The average value $B_{r0dc(av)}$ of DC component of different air gap units, the average value $B_{r01,I/III(av)}$ and $B_{r01,II}$ of fundamental amplitude of air gap unit I, air gap unit III and the fundamental amplitude of air gap unit II, are taken, and the three curves with time are drawn, as shown in Fig. 6. As can be seen from Fig. 6, $B_{r0dc(av)}$ changes approximately sinusoidal with time, and the change period is twice pole distance 2τ . $B_{r01,I/III(av)}$ also approximates the sinusoidal change with time, and the change period is still 2τ . The change of $B_{r01,II}$ with time is approximately a horizontal line, which basically does not change with the change of time.

The distribution of the additional magnetic field in DRCS-PMSM can be summarized from Table II and Fig. 6. The additional magnetic field of DRCS-PMSM exists in the air gap magnetic field of the motor, which contains DC component and AC component. The distribution laws of DC component are as follows: DC component changes sinusoidal periodically with the change of the relative position of the stator and the rotor, and the period is twice of the pole distance; When the rotor is rotated by 0.5τ and 1.5τ , the maximum and minimum values of DC component are obtained respectively. When the rotor is rotated by τ and 2τ , the DC component is 0. The laws of AC component are as

follows: at different times, the fundamental amplitude of AC component of air gap unit I and air gap unit III are the same. With the movement of rotor, the fundamental amplitude also changes sinusoidal periodically, and the period is still twice of the polar distance. The fundamental amplitude of the AC component of the air gap unit II is a constant value, which does not change with the change of the rotor position.

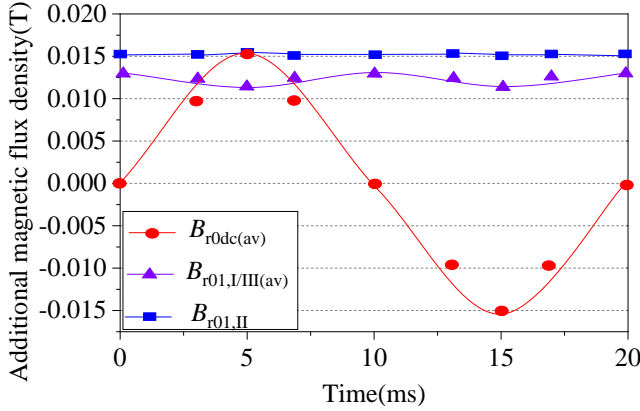


Fig. 6. $B_{r0dc(av)}$, $B_{r0I,III(av)}$ and $B_{r0I,II}$ at different times.

IV. CHARACTERISTIC OF ADDITIONAL MAGNETIC FIELD

A. Source of Additional Magnetic Field

The additional magnetic field of DRCS-PMSM is caused by the change of the flux distribution due to the coupling effect. Fig. 7 shows the distribution of magnetic flux lines of DRCS-PMSM at two typical moments. It can be seen from Fig. 7 that the distribution of magnetic flux lines in the region near the coupling area is obviously different at different moments. The stator core containing slots and windings in the original motor model is defined as the effective core, which is involved in the electromechanical energy conversion, as the part surrounded by black lines in Fig. 7.

When $t=0$ ms, the magnetic flux lines distribution of DRCS-PMSM is shown in Fig. 7(a). For conventional permanent magnet motors that do not have a “coupling effect”, half of the flux emitted by the No. 1 permanent magnet is turned to the No. 2 permanent magnet, and the other half is turned to the No. 8 permanent magnet. However, due to the coupling area, part of the flux emitted by No. 1 permanent magnet is directly linked to No. 2 permanent magnet, and the other part is linked to No. 9 permanent magnet, and then returned to No. 2 permanent magnet through No. 10 permanent magnet or No. 8 permanent magnet through No. 16 permanent magnet. At this time, the magnetic flux emitted by the No. 1 permanent magnet increases the magnetic flux in the effective core by Φ_{u1} . Similarly, the same situation exists for the No. 8 permanent magnet, which increases the magnetic flux in the effective core by Φ_{d1} . Because Φ_{u1} and Φ_{d1} are opposite, the flux change in the entire effective core is 0. According to the number of the magnetic flux lines, half of the flux emitted by No. 1 permanent magnet goes back to No. 2 permanent magnet, and the other half goes back to No. 8 permanent magnet. The above analysis means that the DC

component of the additional magnetic field at $t=0$ ms is 0.

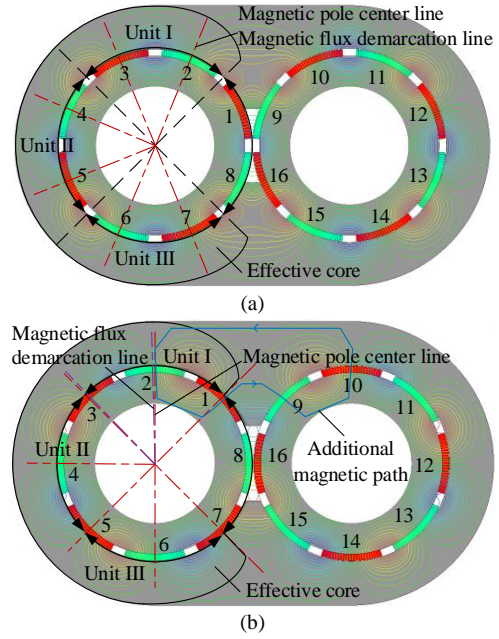


Fig. 7. Magnetic flux lines distribution at two typical moments. (a) $t=0$ ms. (b) $t=5$ ms.

When $t=5$ ms, the magnetic flux lines distribution of DRCS-PMSM is shown in Fig. 7(b). After half of the magnetic flux emitted by No. 1 permanent magnet is directly turned to No. 2 permanent magnet, and the other half of the magnetic flux is turned to No. 9 permanent magnet, most of the magnetic flux passes from No. 16 permanent magnet back to No. 8 permanent magnet. However, a small amount of magnetic flux passes from No. 10 permanent magnet back to No. 2 permanent magnet, as shown by the blue line with arrow in Fig. 7(b). This part increases the magnetic flux in the effective core by Φ_{d2} , and defines this magnetic flux path as an additional magnetic path. Similarly, the same situation exists for the No. 7 permanent magnet, which increases the magnetic flux in the effective core by Φ_{d2} . Because Φ_{u2} and Φ_{d2} are in the same direction, the magnetic flux in the entire effective core increases. This means that there is DC component in the air gap magnetic field when $t=5$ ms, and the DC component is the largest at this time.

Further, the source of AC component in the additional magnetic field is analyzed. The flux flow from a permanent magnet is divided into two directions, each intersecting with its adjacent permanent magnet. In this paper, the demarcation line between the two directions is defined as the magnetic flux demarcation line, as shown in the purple dot line in Fig. 7. The magnetic pole center line for a permanent magnet is drawn, as shown by the red dot line in Fig. 7.

When $t=0$ ms, the magnetic flux demarcation line of the permanent magnet corresponding to the effective core coincides with the magnetic pole center line, so the fundamental component of the AC component is the largest. However, due to the proximity of air gap unit I and III to the coupling area, the magnetic circuit of air gap unit II is obviously different from that of air gap unit I and III. As a

result, the additional magnetic fundamental amplitude of air gap unit II is larger than that of air gap unit I and III.

When $t=5$ ms, the magnetic flux demarcation line of No. 2 permanent magnet in air gap unit I and the magnetic pole center line are greatly offset, resulting in a small shift between the magnetic flux demarcation line and the magnetic pole center line of No. 3 permanent magnet. While the magnetic flux demarcation line of No. 4 permanent magnet in air gap unit II basically coincides with the magnetic pole center line. The same is true for permanent magnets in air gap unit III. It can be inferred that due to the ‘‘coupling effect’’, the angle between the magnetic flux demarcation line and the magnetic pole center line changes periodically with the movement of the rotor, and the fundamental amplitude of the additional magnetic field AC component of the air gap unit I and III is the smallest. The air gap unit II is far away from the coupling area, and the ‘‘coupling effect’’ has little influence on it. This reason makes the fundamental amplitude of the AC component of the additional magnetic field hardly changes with the movement of the rotor.

B. Analytical Model of Additional Magnetic Field

The additional magnetic flux at the upper and lower ends of the DRCS-PMSM coupling area into the effective core is Φ_u and Φ_d , respectively. The amplitude of the two is the same, the phase is different, and the direction is opposite, and both are functions of the rotor position angle θ . The upper additional flux Φ_u and the lower additional flux Φ_d can be expanded into the form of Fourier series, and the expressions are respectively:

$$\Phi_u(\theta) = \Phi_0 + \sum_{n=1}^{\infty} \Phi_{sn} \sin\left(\frac{n\pi}{\tau}\theta\right) + \sum_{n=1}^{\infty} \Phi_{cn} \cos\left(\frac{n\pi}{\tau}\theta\right) \quad (2)$$

$$\Phi_d(\theta) = -\Phi_0 + \sum_{n=1}^{\infty} \Phi_{sn} \sin\left(\frac{n\pi}{\tau}\theta + \delta\right) - \sum_{n=1}^{\infty} \Phi_{cn} \cos\left(\frac{n\pi}{\tau}\theta + \delta\right) \quad (3)$$

where Φ_0 is the average value. Φ_{sn} and Φ_{cn} are the amplitudes of the n -th harmonic. δ is the phase difference between the additional flux at the upper and lower ends. The total additional flux Φ_{total} entering the effective core is:

$$\begin{aligned} \Phi_{total}(\theta) &= \Phi_u(\theta) + \Phi_d(\theta) = \sum_{n=1}^{\infty} 2\Phi_{sn} \left[\sin\left(\frac{n\pi}{\tau}\theta + \frac{\delta}{2}\right) \cos\left(\frac{\delta}{2}\right) \right] + \\ &\quad \sum_{n=1}^{\infty} 2\Phi_{cn} \left[\sin\left(\frac{n\pi}{\tau}\theta + \frac{\delta}{2}\right) \sin\left(\frac{\delta}{2}\right) \right] \\ &= \sum_{n=1}^{\infty} 2\Phi_{an} \sin\left(\frac{n\pi}{\tau}\theta + \frac{\delta}{2}\right) \end{aligned} \quad (4)$$

where Φ_{an} is the amplitude of the n -th harmonic. The expression is:

$$\Phi_{an} = \Phi_{sn} \cos\left(\frac{\delta}{2}\right) + \Phi_{cn} \sin\left(\frac{\delta}{2}\right) \quad (5)$$

B_{r0dc} in the additional magnetic flux density is:

$$\begin{aligned} B_{r0dc}(\theta) &= \frac{\Phi_{total}(\theta)}{S} = \frac{360^\circ}{\pi(360^\circ - \alpha)D_{si}L_{ef}} \Phi_{total}(\theta) \\ &= \sum_{n=1}^{\infty} B_{an} \sin\left(\frac{n\pi}{\tau}\theta + \frac{\delta}{2}\right) \end{aligned} \quad (6)$$

where S is the cross-sectional area of the effective core perpendicular to the direction of the air gap. D_{si} is the inner diameter of the stator core. L_{ef} is the effective length of the stator core. B_{an} is the amplitude of the n -th harmonic. The additional magnetic flux density in the i -th air gap unit, denoted as $B_{r0ac,i}$, can be expressed as:

$$B_{r0ac,i}(\theta, x) = \sum_{n=1}^{\infty} B_{bn,i} \sin\left(\frac{n\pi}{\tau}\theta + \frac{n\pi}{\tau}x + \varphi_{n,i}\right) \quad (7)$$

where $B_{bn,i}$ and $\varphi_{n,i}$ are the amplitude and initial phase of the n -th harmonic in the i th air gap unit, respectively.

According to Table II and Fig. 6, it can be inferred that the AC component of the additional magnetic field in air gap unit I and III has equal amplitude and opposite direction, so:

$$B_{r0ac,I}(\theta, x) = -B_{r0ac,III}(\theta, x) \quad (8)$$

Since the AC component amplitude of the additional magnetic field in the air gap unit II does not change with the change of the rotor position θ , it can be regarded as only related to the relative position x between the stator and the rotor. In this case, (7) can be simplified as:

$$B_{r0ac,II}(x) = \sum_{n=1}^{\infty} B_{bn,II} \sin\left(\frac{n\pi}{\tau}x + \varphi_{n,II}\right) \quad (9)$$

Then the additional magnetic density $B_{r0,i}$ in the i -th air gap unit is expressed as:

$$B_{r0,i}(\theta, x) = B_{r0dc}(\theta) + B_{r0ac,i}(\theta, x) \quad (10)$$

From (4) to (10), it can be seen that the DC component in the additional magnetic field takes 2τ as the fundamental period, which is consistent with the simulation results in Section II. The existence of additional magnetic path changes the magnetic flux in the effective core and causes the magnetic flux density in each air gap unit to produce DC component. At the same time, the existence of additional magnetic path changes the magnetic flux demarcation line in each air gap unit, so that the magnetic flux density in each air gap unit generates an AC component. Therefore, the total additional flux Φ_{total} is very important for the additional magnetic field.

When the coupling angle α , the inner diameter D_{si} of the stator core, and the effective length L_{ef} of the stator core are constant, Φ_{total} is only related to Φ_u and Φ_d . In Fig. 7(b), β and d directly determine the flux path of No. 1 permanent magnet. When d is large, because the magnetic permeability of the core is much larger than that of the air in the duty area, the No. 1 permanent magnet has more flux flowing into the No. 9 permanent magnet, which increases Φ_u . The change of β affects the degree of the magnetic paths coupling between the flux generated by No. 1 permanent magnet and the flux generated by No. 8 permanent magnet, which also changes Φ_u . A similar situation exists for No. 7 permanent magnet, which increases Φ_d . Therefore, β and d determine the additional magnetic path and are the key parameters that affect the additional magnetic field.

C. Influence of Key Parameters on Additional Magnetic Field

The finite element model of DRCS-PMSM is established to explore the influence of key parameters on the additional

magnetic field. It can be seen from Section II that when $t=5$ ms, the additional magnetic flux Φ_{an} entering the effective core is the largest. Fig. 8 shows the variation curve of the DC component B_{r0dc} amplitude of the additional magnetic field with duty angle β and coupling distance d when $t=5$ ms. As can be seen from Fig. 8, the amplitude of B_{r0dc} increases linearly with the increase of d . With the increase of β , the B_{r0dc} amplitude first increases and then decreases. When $\beta=45^\circ$, the B_{r0dc} amplitude reaches a maximum value. This change rule is caused by the change of magnetic path in the coupling area. The AC component of the additional magnetic field is due to the shift of the flux demarcation line caused by the existence of the additional magnetic path, and the additional magnetic path is the reason for the DC component. Therefore, the laws of the influence of key parameters on the DC component amplitude is also applicable to the AC component amplitude.

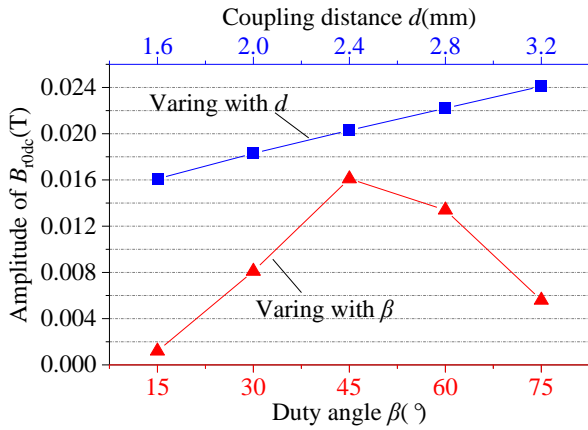


Fig. 8. The curve of DC component varying with the key parameters.

V. INFLUENCE OF ADDITIONAL MAGNETIC FIELD ON ELECTROMAGNETIC TORQUE

A. Analytical Modeling of Additional Torque

The torque generated by the additional magnetic field is defined as the additional torque. The additional torque is superimposed in the electromagnetic torque, which affects the torque performance of the motor. The total additional torque T_{ad} can be regarded as the sum of the additional torque $T_{ad,I}$, $T_{ad,II}$ and $T_{ad,III}$ within the three air gap units, expressed as:

$$T_{ad}(\theta) = T_{ad,I}(\theta) + T_{ad,II}(\theta) + T_{ad,III}(\theta) \quad (11)$$

Suppose that the core permeability is infinite, according to energy method, the torque $T_{ad,i}$ in the i -th air gap unit is:

$$\begin{aligned} T_{ad,i}(\theta) &= \frac{\partial W_i}{\partial \theta} = \frac{1}{2\mu_0} \frac{\partial}{\partial \theta} \int B_{r0i}^2(\theta, x) dV \\ &= \frac{1}{2\mu_0} \frac{\partial}{\partial \theta} \left[\int B_{r0dc}(\theta) + B_{r0ac,i}(\theta, x) \right]^2 dV \\ &= \frac{1}{2\mu_0} \frac{\partial}{\partial \theta} \int B_{r0dc}^2(\theta) dV + \frac{1}{\mu_0} \frac{\partial}{\partial \theta} \int B_{r0dc}(\theta) B_{r0ac,i}(\theta, x) dV + \\ &\quad \frac{1}{2\mu_0} \frac{\partial}{\partial \theta} \int B_{r0ac,i}^2(\theta, x) dV \end{aligned} \quad (12)$$

where W_i is the magnetic field energy stored in the i -th air gap unit. μ_0 is the vacuum permeability.

The first item in (12) is calculated as:

$$\begin{aligned} T_{ad,i-1}(\theta) &= \frac{V_1}{2\mu_0} \frac{\partial}{\partial \theta} \sum_{n=1}^{\infty} B_{an}^2 \sin^2 \left(\frac{n\pi}{\tau} \theta + \frac{\delta}{2} \right) \\ &= \frac{V_1 \pi}{2\mu_0 \tau} \sum_{n=1}^{\infty} n B_{an}^2 \sin \left(\frac{2n\pi}{\tau} \theta + \delta \right) \end{aligned} \quad (13)$$

where V_1 is the volume of an air gap unit.

The second item in (12) is:

$$\begin{aligned} T_{ad,i-2}(\theta) &= \frac{1}{\mu_0} \frac{\partial}{\partial \theta} \int \sum_{n=1}^{\infty} B_{an} \sin \left(\frac{n\pi}{\tau} \theta + \frac{\delta}{2} \right) \times \\ &\quad \sum_{n=1}^{\infty} B_{bn,i} \sin \left(\frac{n\pi}{\tau} \theta + \frac{n\pi}{\tau} x + \varphi_{n,i} \right) dV \\ &= \frac{L_{ef} g}{\mu_0} \frac{\partial}{\partial \theta} \sum_{n=1}^{\infty} B_{an} \sin \left(\frac{n\pi}{\tau} \theta + \frac{\delta}{2} \right) \times \\ &\quad \int_0^{\tau D_{si}} \sum_{n=1}^{\infty} B_{bn,i} \sin \left(\frac{n\pi}{\tau} \theta + \frac{n\pi}{\tau} x + \varphi_{n,i} \right) dx \\ &= \frac{2L_{ef} g}{\mu_0} \sum_{n=1}^{\infty} B_{an} \sin \left(\frac{n\pi}{\tau} \theta + \frac{\delta}{2} \right) \times \\ &\quad \sum_{n=1}^{\infty} B_{bn,i} \left[\cos \left(\frac{n\pi}{\tau} \theta + \frac{n\pi D_{si}}{2} + \varphi_{n,i} \right) \sin \frac{n\pi D_{si}}{2} \right] \\ &\quad + \frac{2L_{ef} g}{\mu_0} \sum_{n=1}^{\infty} B_{an} \cos \left(\frac{n\pi}{\tau} \theta + \frac{\delta}{2} \right) \times \\ &\quad \sum_{n=1}^{\infty} B_{bn,i} \left[\sin \left(\frac{n\pi}{\tau} \theta + \frac{n\pi D_{si}}{2} + \varphi_{n,i} \right) \sin \frac{n\pi D_{si}}{2} \right] \end{aligned} \quad (14)$$

In air gap unit II, (14) can be simplified as:

$$\begin{aligned} T_{ad,II-2}(\theta) &= \frac{2L_{ef} g}{\mu_0} \sum_{n=1}^{\infty} B_{an} \cos \left(\frac{n\pi}{\tau} \theta + \frac{\delta}{2} \right) \times \\ &\quad \sum_{n=1}^{\infty} B_{bn,II} \left[\sin \left(\frac{n\pi D_{si}}{2} + \varphi_{n,II} \right) \sin \frac{n\pi D_{si}}{2} \right] \end{aligned} \quad (15)$$

The third item in (12) is:

$$\begin{aligned} T_{ad,i-3}(\theta) &= \frac{1}{2\mu_0} \frac{\partial}{\partial \theta} \int \sum_{n=1}^{\infty} B_{bn,i}^2 \sin^2 \left(\frac{n\pi}{\tau} \theta + \frac{n\pi}{\tau} x + \varphi_{n,i} \right) dV \\ &= \frac{L_{ef} g}{2\mu_0} \frac{\partial}{\partial \theta} \int_0^{\tau D_{si}} \sum_{n=1}^{\infty} B_{bn,i}^2 \sin^2 \left(\frac{n\pi}{\tau} (\theta + x) + \varphi_{n,i} \right) dx \\ &= \frac{L_{ef} g}{2\mu_0} \sum_{n=1}^{\infty} B_{bn,i}^2 \sin \left(\frac{2n\pi}{\tau} \theta + n\pi D_{si} + 2\varphi_{n,i} \right) \sin n\pi D_{si} \end{aligned} \quad (16)$$

(13) reflects the torque generated by the DC component of the additional magnetic field in DRCS-PMSM, which takes the pole distance τ as the fundamental period and exists in each air gap unit. (14) reflects the influence of DC component on AC component, and the torque generated also is based on a period of the pole distance τ . (16) reflects the torque generated by the AC component of the additional magnetic field, which still takes the pole distance τ as the fundamental period.

It can be concluded from the above analysis that the torque generated by the additional magnetic field in the air gap unit I and III take the pole distance τ as the fundamental period. The torque generated by the additional magnetic field in the air gap unit II has a fundamental period of 2τ . Strictly speaking, the total additional torque takes 2τ as the fundamental period,

but because the torque generated by (15) is relatively small, the total additional torque is more obviously shown as the fundamental period of τ . In addition, the magnitude of the additional torque is related to the additional flux amplitude, that is, the structural parameters of the magnetic circuit in the coupling area.

B. Finite Element Simulation Verification

The additional torque cannot be obtained directly through simulation. In order to verify the influence of the additional magnetic field on the electromagnetic torque, the additional torque separation model as shown in Fig. 9 is established in this paper, and the whole circle where the outer diameter of the stator core is located is set as the vector magnetic potential boundary condition. Model I contains 3 unit-motors and model II contains 2 unit-motors. It should be noted that the finite element simulation model in Fig. 9 also has an additional magnetic field, and its generation mechanism is the same as the analysis in Section IV. There is only end-effect torque T_{end} and additional torque T_{ad} in this model, which can replace the verification of the periodic rule of additional torque in DRCS-PMSM. The additional torque in the two cases is only different in amplitude.

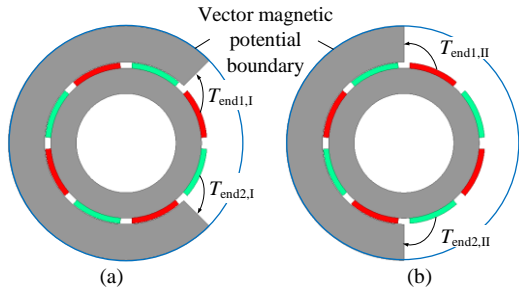


Fig. 9. Additional torque separation models. (a) Model I. (b) Model II.

The process of separating the additional torque is as follows. In Fig. 9, the torque T_I and the torque T_{II} of model I and model II are respectively:

$$\begin{cases} T_I(\theta) = T_{\text{ad},I}(\theta) + T_{\text{end},I}(\theta) + T_{\text{end},I}(\theta) \\ T_{II}(\theta) = T_{\text{ad},II}(\theta) + T_{\text{end},II}(\theta) + T_{\text{end},II}(\theta) \end{cases} \quad (17)$$

where $T_{\text{ad},I}$, $T_{\text{end},I}$ and $T_{\text{end},I}$ are the additional torque, upper end effect torque and lower end effect torque of model I respectively. $T_{\text{ad},II}$, $T_{\text{end},II}$, and $T_{\text{end},II}$ are the additional torque, upper end effect moment, and lower end effect moment of model II, respectively. According to the linear motor theory, we can know:

$$\begin{cases} T_{\text{end},I}(\theta) = T_{\text{end},II}(\theta) \\ T_{\text{end},I}(\theta) = T_{\text{end},I}(\theta + 2\tau) = T_{\text{end},II}(\theta) \end{cases} \quad (18)$$

According to (4)-(6), the B_{an} of additional magnetic field of model I and model II satisfies the following equation:

$$\frac{B_{\text{an},I}}{B_{\text{an},II}} = \frac{\Phi_{\text{total}}(\theta) / S_I}{\Phi_{\text{total}}(\theta) / S_{II}} = \frac{2}{3} \quad (19)$$

In combination with (12), the relationship between $T_{\text{ad},I}$ and $T_{\text{ad},II}$ is:

$$\frac{T_{\text{ad},I}}{T_{\text{ad},II}} = \frac{2}{3} \quad (20)$$

From (17)-(20), the additional torque in model I is:

$$T_{\text{ad},I}(\theta) = 2[T_{II}(\theta) - T_I(\theta)] \quad (21)$$

Fig. 10 shows the additional torque. As can be seen from Fig. 10, the peak-to-peak value of additional torque is 2.5 N m and has obvious periodicity. The Fourier decomposition of the pole distance τ as the fundamental period shows that the fundamental wave occupies the largest proportion with a amplitude of 0.71 N m, followed by the second harmonics with a amplitude of 0.28 N m, in addition to a small number of multiple harmonics. The fluctuation rule of additional torque in Fig. 10 is consistent with the summary rule in the last paragraph of Section A.

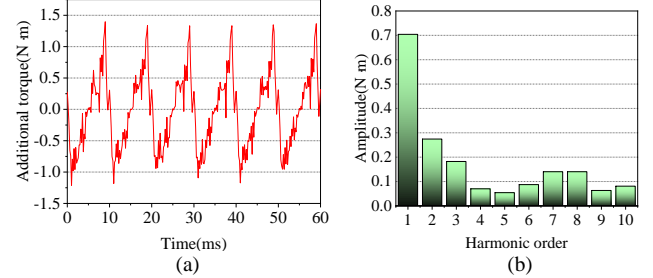


Fig. 10. Additional torque. (a) Waveform. (b) Harmonic analysis.

VI. PROTOTYPE TEST VERIFICATION

The main means studied in Sections III to V depend on the finite element simulation models, so the accuracy of the finite element simulation models is crucial. In order to verify the accuracy of the finite element model, a DRCS-PMSM prototype is developed.

The change of the air gap magnetic field in the motor induces the back electromotive force in the windings, so the accuracy of the back electromotive force can reflect the accuracy of the air gap magnetic field, and the back electromotive force is easier to measure. In order to ensure the synchronization of the rotation of the two rotors, two mechanical gears are installed at the end of the two rotating shafts. An electric wrench is used to drag a rotor at the other end of the shaft to rotate, at which time the two rotors rotate simultaneously, and an oscilloscope is used to record the no-load back electromotive force of the motor. The test platform is shown in Fig. 11.

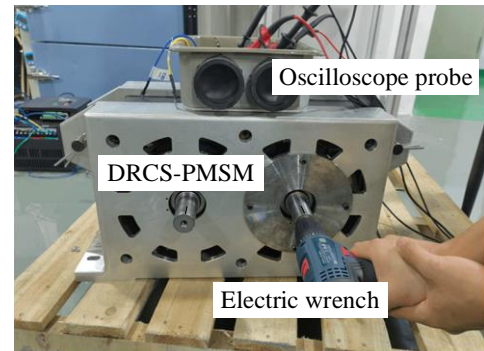


Fig. 11. No-load back EMF test platform.

The drag speed of the electric wrench is 280 r/min, and the back electromotive force waveform intercepted by the

oscilloscope is shown in Fig. 12. It can be seen from Fig. 12 that the waveform of no-load back electromotive force is in good agreement. The test result of the RMS of the no-load back electromotive force in phase A is 76.33 V, and the simulation result is 78.25 V, with a deviation of 2.45%. Considering the machining error and testing error, it can be considered that the two are approximately the same, which proves the accuracy of the finite element simulation model in this paper.

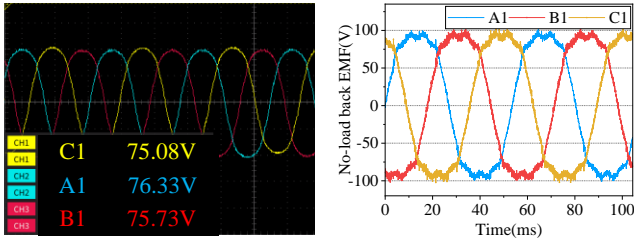


Fig. 12. No-load back EMF. (a)Tested. (b) Simulated.

The load test platform is shown in Fig. 13. In order to facilitate measurement, the mechanical gears are used to transfer the output power of two rotating shafts to one shaft. A magnetic powder brake is used to apply the load to DRCS-PMSM. The output torque of the shaft is recorded by the dynamic torque sensor. Fig. 14 shows the waveforms of load torque under both simulation and test conditions. As can be seen from Fig. 14, the average torque obtained by simulation is the same as that obtained by test, and the fluctuation rules of the two waveforms are approximately the same. However, due to the synchronous mechanical gears, the torque ripple obtained by the test is relatively small. Load is gradually applied to the motor, and output torque and corresponding current are recorded. The relationship curve is shown in Fig. 15. It can be seen from Fig. 15 that the output torque of the motor is basically linear with the input current. When the input current is about 19 A, the output torque can reach 140 N m, indicating that the motor can drive the rated load. The output torque is converted into the output power, and a power analyzer is used to measure the input power of the motor. The efficiency of the motor can be obtained by calculating the ratio of the output power to the input power, which is about 92.8%.

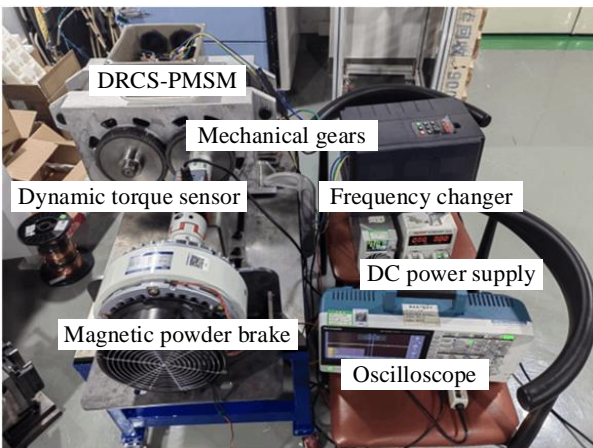


Fig. 13. Load performance test platform.

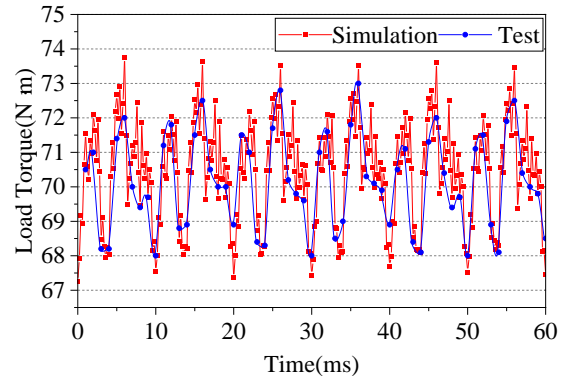


Fig. 14. Waveforms of load torque under both simulation and test conditions.

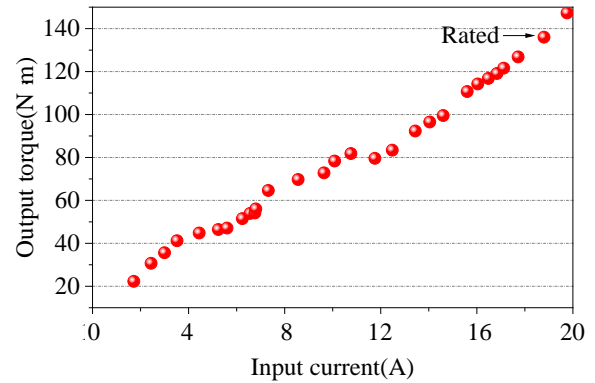


Fig. 15. The relationship between the output torque and the input current.

VII. CONCLUSION

In this paper, the additional magnetic field of DRCS-PMSM and its influence on electromagnetic torque are studied, which brings fluctuations to the electromagnetic torque of the motor. The main conclusions of this paper are as follows:

- 1) The additional magnetic circuit generates an additional magnetic field in the air gap magnetic field of the motor, and the additional magnetic field contains not only the DC component, but also the AC component. The DC component in each air gap unit is equal, and the DC component amplitude changes periodically with the change of rotor position, and the period is twice of the pole distance. The AC components in the air gap unit I and the air gap unit III are equal, and the fundamental amplitude of the AC component also changes periodically with the change of the rotor position, and the period is still twice of the pole distance.
- 2) The additional magnetic field produces the additional torque, which increases the torque ripple of the motor. The additional torque is more obviously reflected in the pole distance as the period, which has the largest proportion of fundamental wave and second harmonic wave. As key parameters, duty angle and coupling distance affect the amplitude of additional magnetic field and additional torque. Reasonable design of duty angle and coupling distance can reduce the additional torque of the motor, which further reveal and perfect the internal mechanism that optimizing the coupling structure can reduce the torque ripple.

REFERENCES

- [1] S. R. Dai, G. H. Feng, and W. Li *et al*, "Analytical No-load Magnetic Field Model Taking Account of the Curvature Coefficient for Parallel Direct-driven Conjoined Permanent Magnet Synchronous Motor," *IEEE Transactions on Electrical and Electronic Engineering*, vol. 17, no. 1, pp. 26–36, Jan. 2022.
- [2] Y. Chen, D. J. Tao, and B. J. Ge *et al*, "Load Torque Weakening of Dual-parallel Rotor Permanent Magnet Motor Based on Torque Harmonic Analysis and Auxiliary Slots," in *Proc. of 2024 IEEE 7th International Electrical and Energy Conference (CIEEC)*, Harbin, China, May 2024, pp. 89–94.
- [3] J. X. Li, C. Di, and X. H. Bao, "Efficiency Improvement for Submersible Motors by Optimizing the Ratio of Diameter to Shaft Length," *IEEE Transactions on Magnetics*, vol. 58, no. 2, pp. 1–6, Feb. 2022.
- [4] Y. D. Song, G. W. Liu, and S. Y. Yu *et al*, "Investigation of a Low-speed High-torque-density Direct-drive External-rotor PMSM for Belt Conveyor Application," *IEEE Access*, vol. 11, pp. 110479–110489, Sept. 2023.
- [5] J. X. Zhang, B. Y. Zhang, and D. M. Li *et al*, "Research on Cogging Torque Weakening of Direct-drive Permanent Magnet Motor with Inner Enhance Force," *IEEE Transactions on Electrical and Electronic Engineering*, vol. 17, no. 2, pp. 160–168, Feb. 2022.
- [6] S. N. Wu, Z. M. Li, and W. M. Tong, "Research on Thermal Calculation and End Winding Heat Conduction Optimization of Low Speed High Torque Permanent Magnet Synchronous Motor," *CES Transactions on Electrical Machines and Systems*, vol. 7, no. 4, pp. 397–403, Dec. 2023.
- [7] Y. L. Yu, Y. L. Pei, and F. Chai *et al*, "Performance Comparison Between Permanent Magnet Synchronous Motor and Vernier Motor for In-wheel Direct Drive," *IEEE Transactions on Industrial Electronics*, vol. 70, no. 8, pp. 7761–7772, Aug. 2023.
- [8] Z. Y. Liu, B. Y. Zhang, and Y. Hu *et al*, "Design and Analysis of Concave-core Stator Direct-drive Permanent Magnet Motor," *IET Electric Power Applications*, vol. 17, no. 9, pp. 1182–1196, Sept. 2023.
- [9] S. R. Dai, B. Y. Zhang, and W. Li *et al*, "A Parallel Direct-driven Permanent Magnet Synchronous Motor with Stator Connected Dual-rotors Synchronous," *Transactions of China Electrotechnical Society*, vol. 35, no. 10, pp. 2107–2118, May 2020.
- [10] Y. Chen, D. J. Tao, and L. K. Wang *et al*, "Mechanism and Suppression of Torque Ripple of Dual-parallel Rotor Permanent Magnet Synchronous Motor," *Transactions of China Electrotechnical Society*, vol. 39, no. 20, pp. 6357–6370, Oct. 2024.
- [11] D. J. Tao, Y. Chen, and Z. Li *et al*, "Analysis and Optimization of Unbalanced Electromagnetic Force on the Rotor of Dual-parallel Rotor Permanent Magnet Direct-driven Motor," *Transactions of China Electrotechnical Society*, vol. 39, no. 10, pp. 2961–2973, May 2024.
- [12] Y. Chen, D. J. Tao, and S. P. Li *et al*, "Optimization Design of Dual-parallel Rotor Permanent Magnet Motor Based on Dynamic Kriging Surrogate Model," *IEEE Transactions on Electrical and Electronic Engineering*, vol. 20, no. 1, pp. 127–137, Jan. 2025.
- [13] B. C. Guo, Y. L. Du, and F. Peng *et al*, "Magnetic Field Calculation in Axial Flux Permanent Magnet Motor with Rotor Eccentricity," *IEEE Transactions on Magnetics*, vol. 58, no. 9, pp. 1–4, Sept. 2022.
- [14] Z. Ding, X. Z. Wu, and C. T. Chen *et al*, "Magnetic Field Analysis of Surface-mounted Permanent Magnet Motors Based on an Improved Conformal Mapping Method," *IEEE Transactions on Industry Applications*, vol. 59, no. 2, pp. 1689–1698, Mar.-Apr. 2023.
- [15] B. Ladghem-Chikouche, K. Boughrara, and F. Dubas *et al*, "Semi-analytical Magnetic Field Calculation for Dual-rotor Permanent-magnet Synchronous Machines by Using Hybrid Model," *IEEE Transactions on Magnetics*, vol. 58, no. 1, pp. 1–10, Jan. 2022.
- [16] H. Zhou, X. H. Wang, and W. L. Zhao *et al*, "Magnetic Field Calculation of the U-shaped Interior Permanent-magnet Synchronous Machine Considering the Parallel Magnetization and Bridge Saturation," *IEEE Transactions on Industrial Electronics*, vol. 71, no. 10, pp. 11817–11828, Oct. 2024.
- [17] X. Chen, W. D. Pan, and X. F. Wang, "Analytical Calculation of Air-gap Magnetic Field in Brushless Doubly-fed Reluctance Machine with Flux Barriers," *IEEE Transactions on Energy Conversion*, vol. 37, no. 2, pp. 1292–1303, Jun. 2022.
- [18] Q. Wang, Y. L. Yang, and P. C. Ma *et al*, "Analysis and Suppression of Phase Unbalance Induced Force Ripples in Permanent Magnet Linear Motors," *IEEE Access*, vol. 10, pp. 5416–5423, Jan. 2022.
- [19] B. H. B. Boff, P. R. Eckert, and Y. Amara, "A Comprehensive Review on the End Effects of Linear Permanent Magnet Machines," *IEEE Transactions on Industry Applications*, vol. 59, no. 2, pp. 1728–1741, Mar.-Apr. 2023.
- [20] Y. T. Zhao, Y. X. Li, and Q. F. Lu, "An accurate No-load Analytical Model of Flat Linear Permanent Magnet Synchronous Machine Accounting for End Effects," *IEEE Transactions on Magnetics*, vol. 59, no. 1, pp. 1–11, Jan. 2023.
- [21] Q. Tan, M. Y. Wang, and L. Y. Li *et al*, "Pulsating Magnetic Field of Permanent Magnet Linear Synchronous Motor and Its Influence on Detent Force," *IEEE Transactions on Energy Conversion*, vol. 36, no. 2, pp. 703–712, Jun. 2021.



Yang Chen received the B.S. and M.S. degrees from Shenyang University of Technology, Shenyang, China, in 2018 and 2021. He is currently pursuing the Ph.D. degree in electrical engineering from Harbin University of Science and Technology, Harbin, China. His research interests include the theory and application technology of electrical machines.



Dajun Tao received the B.S., M.S., and Ph.D. degrees from Harbin University of Science and Technology, Harbin, China, in 2005, 2008, and 2013. He is currently a professor at the Harbin University of Science and Technology. His research interests include the basic theory and application technology of large electrical machines, design and analysis of new special electrical machines, and diagnosis of electrical machines and system faults.



Baojun Ge received the B.S. and M.S. degrees from Harbin University of Science and Technology, Harbin, China, in 1982 and 1985. He received the Ph.D. degrees from Harbin Institute of Technology, Harbin, China, in 1999. He is currently a professor at the Harbin University of Science and Technology. His research interests include the large and special electrical machines, and new technologies for power generation.